International Journal of Power Electronics and Drive System (IJPEDS)
Vol. 17, No. 1, March 2026, pp. 438~452
ISSN: 2088-8694, DOI: 10.11591/ijpeds.v17.i1.pp438-452

A novel technique for induction heating dryer with temperature and voltage control for power inverter

Jeerapong Srivichai, Kittaya Somsai, Akkachai Phuphanin, Nithiroth Pornsuwancharoen
Department of Electrical Engineering, Faculty of Industry and Technology,
Rajamangala University of Technology Isan, Phang Khon, Thailand

Article Info

Article history:

Received Mar 22, 2025
Revised Oct 21, 2025
Accepted Dec 11, 2025

Keywords:

Energy efficiency
Hysteresis control
Induction heating dryer
Phase-shifted PWM
Precise temperature control

ABSTRACT

This study presents a novel prototype of an induction heating dryer integrating hysteresis control with phase-shifted pulse width modulation (PWM) for the first time. The system replaces conventional resistance heating, improving energy efficiency and thermal stability. The 2 kW prototype comprises a drying chamber and a hot air unit with controlled airflow of 1.5 m/s. Phase angle adjustment reduces voltage, current, and power consumption while maintaining the power factor within acceptable limits. The temperature control maintains stability within ±1 °C of the setpoint. The results demonstrate fast, energy-efficient, and precise drying, offering potential benefits for food processing and textile industries, and providing a foundation for future development of intelligent, energy-efficient induction dryers.

Corresponding Author:

Nithiroth Pornsuwancharoen
Department of Electrical Engineering, Faculty of Industry and Technology
Rajamangala University of Technology Isan
Sakon Nakhon Campus, Phang Khon, Sakon Nakhon 47160, Thailand
Email: nithiroth.po@rmuti.ac.th

1. INTRODUCTION

Drying processes are fundamental to a wide range of industries, including food preservation, pharmaceuticals, textiles, and material processing [1]. Precise temperature control during drying is crucial not only for maintaining product quality [2] but also for optimizing energy efficiency [3]. Conventional hot-air drying systems [4], however, often suffer from uneven heat distribution [5], excessive energy consumption [6], and limited adaptability under diverse operating conditions [7]. Recent research has investigated various advanced approaches to overcome these challenges, such as improved drying technologies [8], induction heating methods [9], and the implementation of feedback control strategies [10]–[12].

Although these advances have improved drying performance, significant limitations remain. Hot-air systems are inherently constrained by slow heat transfer and energy inefficiency. Even when induction heating is introduced, most studies have addressed only heat generation without integrating advanced real-time regulation. Similarly, feedback control has been applied to thermal systems, but its systematic integration with induction-based dryers is still lacking. Consequently, there is a clear gap in combining both high-frequency induction heating and advanced control methods in a single, effective drying system.

To address this gap, the present study introduces a novel induction-based drying prototype that integrates high-frequency induction heating with advanced control mechanisms, specifically hysteresis control combined with phase-shifted pulse width modulation (PWM). This integration enables real-time, precise thermal regulation within the drying chamber while ensuring stable and uniform heat distribution. The proposed system delivers three major benefits. First, it enhances drying efficiency by accelerating heat transfer, significantly reducing production time compared to hot-air drying alone [13]. Second, it safeguards product quality [14]–[16] by minimizing risks such as burning, discoloration, or nutrient degradation, which is particularly advantageous in sensitive industries like food and pharmaceuticals. Third, it reduces energy costs and environmental impact [17], [18] while offering compatibility with renewable energy integration for sustainable industrial operation.

Therefore, the objective of this study is to design, develop, and evaluate a high-frequency induction drying system that combines hysteresis control and phase-shifted PWM to achieve precise and sustainable temperature regulation. This integrated control approach addresses the limitations of traditional drying methods by minimizing thermal fluctuations and optimizing power efficiency. By harmonizing these advanced electronic techniques, the proposed system ensures consistent product quality while reducing overall operational costs. Moreover, the research not only advances the state of drying technology but also demonstrates transformative potential across multiple industrial sectors, including food processing, pharmaceuticals, and textiles, where energy-efficient, high-quality, and environmentally responsible drying solutions are increasingly in demand.

2. THEORY AND BACKGROUND

Induction heating has emerged as an efficient and controllable thermal energy source for industrial drying processes [19]–[22]. Unlike conventional convective or resistive heating, induction heating is contactless, enabling rapid energy transfer with high power density and improved energy utilization. In an induction heating dryer, an alternating current flows through the induction coil, producing a time-varying magnetic field that penetrates the conductive workpiece and induces eddy currents. The resistive dissipation of these currents generates heat directly inside the material, enhancing both uniformity and drying efficiency.

2.1. Fundamentals of induction heating for drying processes

The induced heating phenomenon is governed by Maxwell's equations [23]:

$$\nabla \times \vec{E} = -\frac{\partial \vec{B}}{\partial t} \tag{1}$$

$$\nabla \times \vec{H} = \vec{J} + \frac{\partial \vec{D}}{\partial t} \tag{2}$$

where the induced current density is related to the electric field and the material's electrical conductivity:

$$\vec{J} = \sigma \vec{E} \tag{3}$$

The skin depth determines the penetration of the induced current into the material:

$$\delta = \sqrt{\frac{2}{\omega\mu\sigma}} \tag{4}$$

where $\vec{J}$ is the induced current density in the workpiece, σ is the electrical conductivity, δ is the skin depth indicating current penetration, ω is the angular frequency of the excitation, and μ is the magnetic permeability of the material.

While these equations describe the fundamental heating mechanism, the actual electrical power required is estimated in the next section, linking the input power to the thermal energy delivered to both the workpiece and air. This transition from theoretical heating principles to power estimation is crucial for evaluating the overall energy efficiency of the induction system. By accounting for losses in the surrounding medium and the specific heat capacity of the target material, a more precise power profile can be established. Consequently, this comprehensive analysis ensures that the induction system is not only theoretically sound but also practically optimized for high-performance industrial drying.

2.2. Energy relationship

The thermal power required to heat the air can be estimated by (5):

$$Q = \dot{m} c_p \Delta T \tag{5}$$

where Q is the thermal energy of the hot air (kW), c_p is the specific heat of air, ΔT is the temperature difference between the inlet and outlet air (°C), and $\dot{m}$ is the air mass flow rate (kg/s).

$$\dot{m} = \rho \upsilon A \tag{6}$$

where ρ is the air density (kg/m^3), υ is the air velocity (m/s), and A is the cross-sectional area of the air duct (m^2) [24]. The electrical power input considering system efficiency η is

$$P_{in} = Q/\eta \tag{7}$$

This framework allows estimation of required electrical power and supports the design and optimization of induction heating dryers for efficient energy use.

3. RESEARCH METHOD

3.1. Integrated design of induction heating systems

The parameters of the hot-air drying chamber are summarized in Table 1. Under these conditions, a 2.45 kW heater was selected to provide sufficient energy for achieving the target drying temperature, as calculated by (5) and referenced in Figure 1. The chosen airflow of 1.5 m/s ensures efficient heat transfer while minimizing mechanical stress on the agricultural products [22].

Table 1. Operating parameters of the hot air chamber

Parameter	Value (Unit)
Chamber dimensions	0.75 × 0.62 × 0.21 m³
Cross-sectional area (A)	0.04 m²
Air density (ρ)	1.22 kg/m³
Airflow velocity (υ)	1.5 m/s
Mass flow rate ($\dot{m}$)	0.074 kg/s
Temperatures (T_h / T_o)	55 °C / 30 °C
Thermal energy (Q)	2.24 kW

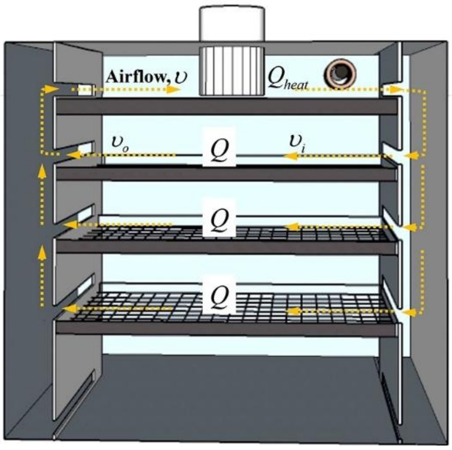

Figure 1. Illustration of the hot air generation system using induction heating

3.2. Control design and implementation of high-frequency power inverters

3.2.1. Theoretical control strategies

The series-resonance full-bridge inverter circuit, shown in Figure 2(a), operates with a DC input voltage and employs a phase-shifted control method [25], [26] for power regulation. The high-frequency output voltage of the inverter is controlled by adjusting the phase shift (ϕ) between one pair of switches (S_1, S_4 or S_2, S_3). The phase shift ranges from 0 (maximum power transfer) to π (minimum power transfer), as illustrated in Figure 2(b). The inverter functions in six distinct operational modes, each critical for regulating power transfer to the load:

- Mode 1 (t_1–t_2): S_1 and S_4 conduct, directing current i_o into the series-resonant output circuit.
- Mode 2 (t_2–t_3): S_1 ceases conduction while i_o continues through S_4, maintaining efficient transfer.
- Mode 3 (t_3–t_4): S_2 conducts, and current flows through diode D_{s2} under zero-voltage switching to minimize losses.

- Mode 4 (t_4–t_5): S_4 stops conducting, ensuring smooth mode transition and system stability.
- Mode 5 (t_5–t_6): i_o flows through D_{s2} with S_3 conducting under ZVS, optimizing efficiency.
- Mode 6 (t_6–t_7): S_2 and S_3 conduct simultaneously, feeding i_o into the series-resonant circuit.

From t_4 to t_{10}, the circuit mirrors the turn-on phase with reversed current, enabling bidirectional power transfer. These principles, combined with hysteresis feedback control [27]–[29] form the foundation for designing the feedback-controlled induction heating dryer for industrial applications.

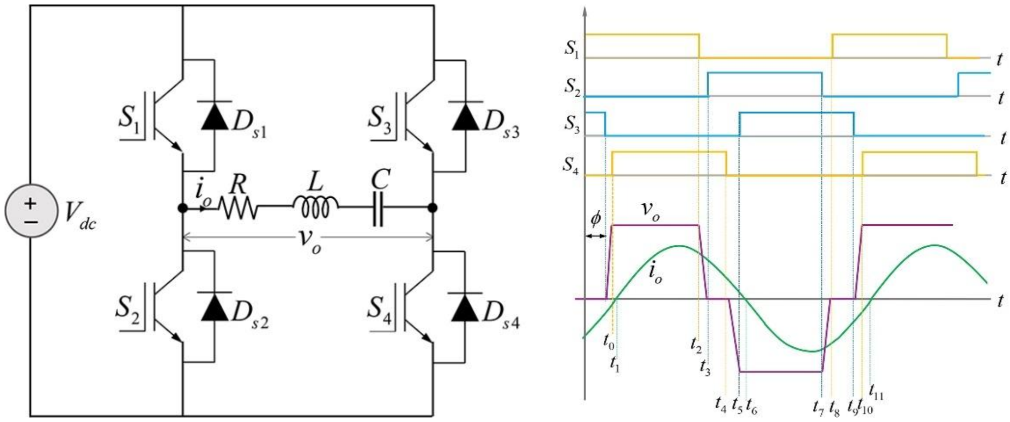

(a) (b)

Figure 2. Phase-shift PWM-controlled series-resonant full-bridge inverter: (a) circuit configuration; (b) phase-shift control waveform

3.2.2. Implementation for temperature and voltage control

The temperature control mechanism employing phase-shift and hysteresis control is illustrated in Figure 3(a), while the operational principle of the proposed system is depicted in Figures 3(b) and 3(c). This figure presents the gate signals of the full-bridge inverter switches S_1–S_4, the phase-shift of the output voltage, and the resulting output voltage waveform v_o generated by the phase-shifting scheme. During operation, the left-side switches (S_1, S_2) and the right-side switches (S_3, S_4) are controlled to operate in complementary pairs, with a dead-time inserted between the switching of each pair to prevent shoot-through. The phase difference ϕ between the two bridge legs determines the inverter's average output voltage, which can be expressed mathematically as (8).

$$v_{o,avg} = V_{dc}\,(1-\phi/\pi),\ 0 \le \phi \le \pi \tag{8}$$

When $\phi = 0$, the two bridge legs operate in phase, resulting in the maximum output voltage and the highest heat delivery. Conversely, when $\phi = \pi$ rad the two bridge legs operate in anti-phase, leading to a zero average output voltage and a complete stop of power delivery.

The control system relies on temperature measurement from a K-type thermocouple installed inside the drying chamber. The measured values are processed by a digital temperature controller, which generates control signals for the inverter circuit. A hysteresis-based control strategy is employed, with the reference temperature set at $T_h{}^* = 55$ ºC and the hysteresis band defined as $\Delta T = \pm 1$ °C, as expressed in (17).

$$\phi = \begin{cases} 0 & ;\ T_h < (T_h{}^* - \Delta T) \\ \pi/2 & ;\ T_h \ge (T_h{}^* + \Delta T) \end{cases} \tag{9}$$

Specifically, when the actual temperature T_h falls below the lower bound ($T_h{}^* - \Delta T = 54$ ºC) the controller sets the phase angle to $\phi = 0$ rad in order to increase heat delivery. In contrast, when the temperature exceeds the upper bound ($T_h{}^* + \Delta T = 56$ ºC), the controller sets the phase angle to $\phi = \pi$, thereby reducing the output voltage nearly to zero and ceasing the heating process. Within the hysteresis range [54 ºC, 56 ºC], the system maintains its current operating state to minimize unnecessary switching transitions. This approach ensures stable temperature regulation within the specified range, suppresses temperature fluctuations, and preserves the inverter's power conversion efficiency.

3.2.3. Simulation setup

To investigate and evaluate the suitability of the power supply for metal heating, a system model was developed using engineering software, as shown in Figure 4. The model comprises a rectifier, full-bridge inverter, impedance-matching transformer (IMT), and RLC resonant tank. The IMT enhances current density and provides galvanic isolation between the power source and the load [30]. The various parameters are presented in Table 2, and the simulation was carried out using a series-resonant inverter model controlled by phase-shift and hysteresis strategies to examine its dynamic behavior. A 150 V DC-link was applied, and the IGBT switches were driven by a PWM signal at 20 kHz with a 48 % duty cycle. The switching angles of (S_1, S_4) and (S_2, S_3), as shown in Figure 4, were varied from 0° to 90° to observe the inverter output voltage and the secondary current of the transformer. Within the hysteresis range [54 ºC, 56 ºC], the system maintains its current operating state to minimize unnecessary switching transitions. This approach ensures stable temperature regulation within the specified range, suppresses temperature fluctuations, and preserves the inverter's power conversion efficiency

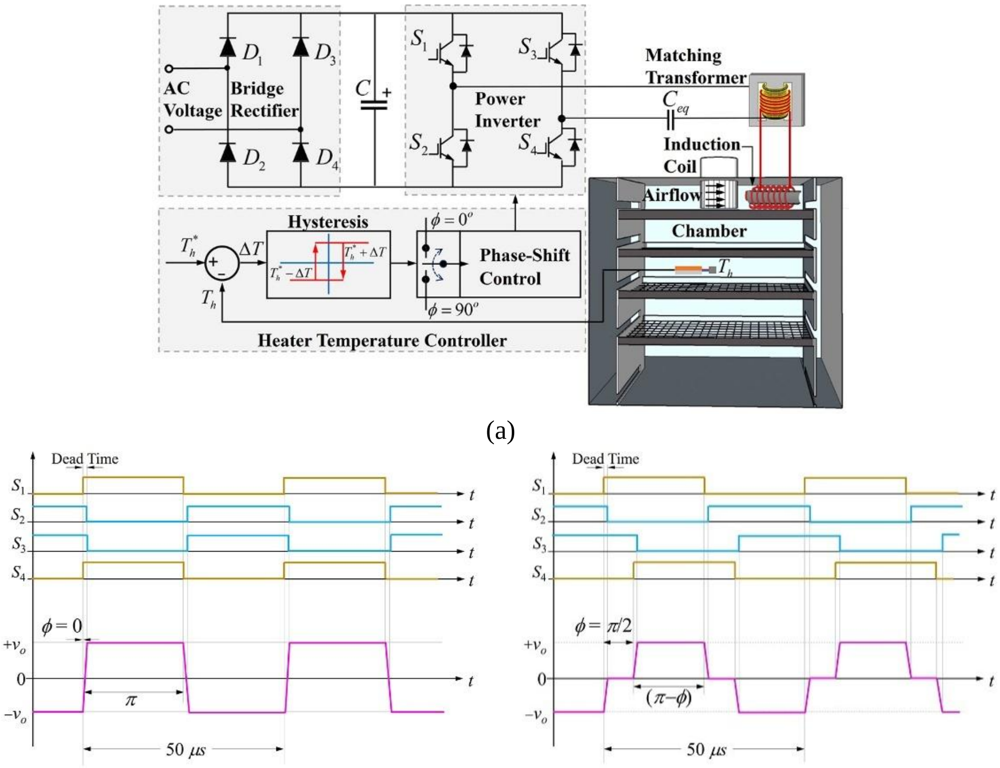

(a)

(b)

(c)

Figure 3. Implementation of the induction heating system with PWM phase-shift feedback control illustrating (a) the system schematic and control block diagram, (b) switching waveforms at $\phi = 0$, and (c) switching waveforms at $\phi = \pi/2$

Figure 3 system architecture and control signal characteristics of the high-frequency induction drying system featuring a feedback-driven PWM phase-shift mechanism. This figure illustrates the integration of the power electronics stage with the thermal control logic to achieve precise temperature regulation within the drying chamber. The comprehensive details include as shown in Figure 3(a) the overall block diagram of the power inverter and heater temperature controller, then Figure 3(b) the PWM switching signals and output voltage at zero phase shift ($\phi = 0$), and Figure 3(c) the modified pulse waveforms when a phase shift is applied ($\phi = \pi/2$). By analyzing these waveforms, the relationship between the control logic and the resulting electrical output used for induction heating can be clearly understood.

The operational characteristics and switching dynamics of the inverter described in Figure 4 are illustrated in Figures 5–8. To provide a comprehensive context for the performance analysis, the waveforms are categorized into three parts: Figures 5(a)–8(a) present the PWM gate signals for S_1 (orange) and S_2 (blue), Figures 5(b)–8(b) display the corresponding signals for S_3 (blue) and S_4 (orange) with phase-shift increments of 0º, 30º, 60º, and 90°, respectively, and Figures 5(c)–8(c) demonstrate the resulting inverter output voltage (v_o, purple) and secondary current (i_o, dark green). The quantitative performance data derived from these waveforms are summarized in Table 3, which lists the RMS values for output voltage ($v_{o,rms}$), output current ($i_{o,rms}$), and output power ($P_{o,rms}$) across the different phase-shift conditions. As shown in Figure 5 and Table 3, the system achieves its maximum output at a 0º phase angle, with an output voltage of 149.9 V and a secondary current of 28.04 A. As the phase angle increases to 30º, 60º, and 90º (Figures 6–8), the output voltage decreases to 135.1 V, 120.3 V, and 103.9 V, while the secondary current of 26.85 A, 23.79 A, and 19.22 A, respectively. These results clearly demonstrate that increasing the phase angle between S_3–S_4 and S_1–S_2 results in a proportional decrease in both inverter output voltage and secondary current, which is consistent with the expected phase-shift behavior of the series-resonant inverter system.

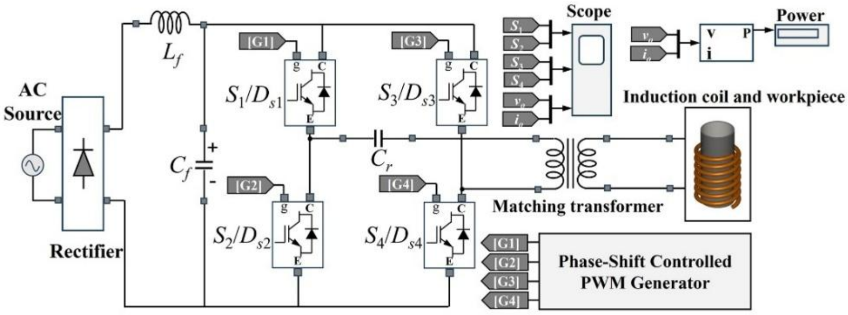

Figure 4. Simulation of RLC resonant circuit

Table 2. Electrical parameters used in the simulation

	Description	Symbol	Value	Reference
DC-link	Inductance filter	L_f	220 μF	[31], [32]
	Capacitance filter	C_f	0.94 mH	[31], [32]
Matching Transformer specifications	Transformer core	Ferrite	-	
	Primary turns	N_p	20	
	Secondary turns	N_s	2	
	Transformer ratio	n	10	
Induction coil workpiece	Equivalent inductance	L_{eq}	2.5 μH	[33]
	Equivalent resistor	R_{eq}	0.048 Ω	[33]
Matching transformer	Equivalent inductance	L'_{eq}	0.25 mH	[33]
	Equivalent resistor	R'_{eq}	4.81 Ω	[33]
	Tank capacitor	C_r	0.25 μF	[33]
	Quality factor	Q	6.53	
	Resonant frequency	f_r	20 kHz	[34], [35]

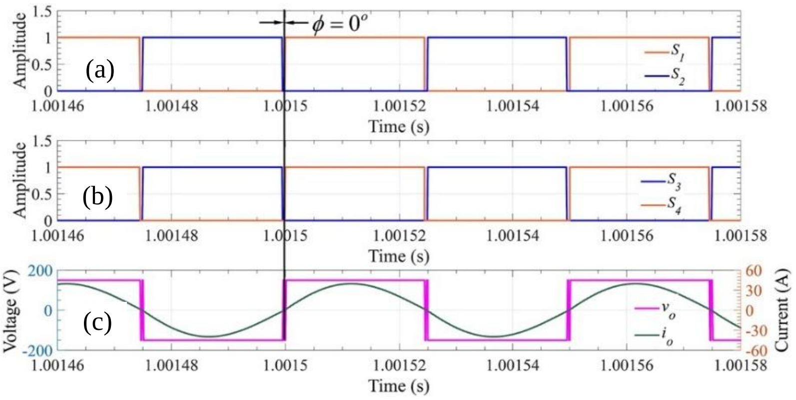

Figure 5. Inverter output voltage and current waveforms at a PWM phase angle of 0°, showing (a) gate signals S_1, S_2, (b) gate signals S_3, S_4, and (c) output voltage (v_o) and current (i_o)

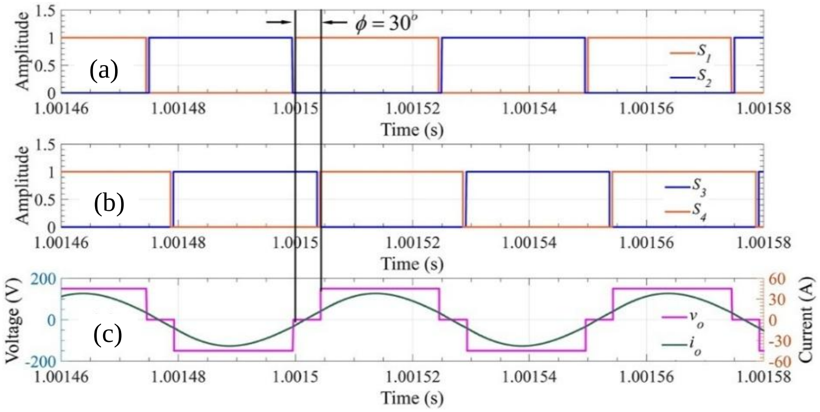

Figure 6. Inverter output voltage and current waveforms at a PWM phase angle of 30° showing (a) gate signals S_1, S_2 (b) gate signals S_3, S_4, and (c) output voltage (v_o) and current (i_o)

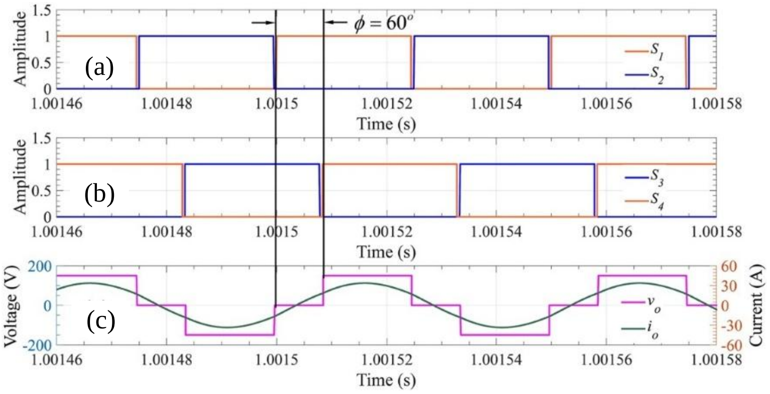

Figure 7. Inverter output voltage and current waveforms at a PWM phase angle of 60° showing (a) gate signals S_1, S_2 (b) gate signals S_3, S_4, and (c) output voltage (v_o) and current (i_o)

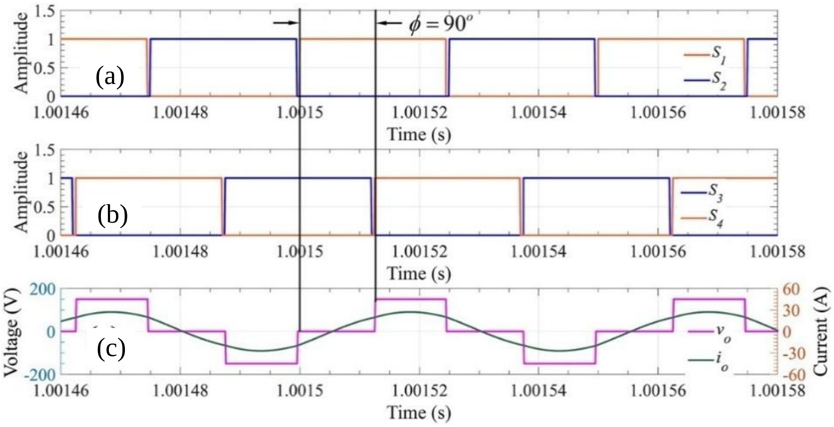

Figure 8. Inverter output voltage and current waveforms at a PWM phase angle of 90°, showing (a) gate signals S_1, S_2 (b) gate signals S_3, S_4, and (c) output voltage (v_o) and current (i_o)

Table 3. Simulation results

Figure	PWM phase shift (o)	Inverter output voltage $v_{o,rms}$(V)	Inverter output current $i_{o,rms}$(A)	Inverter output power $P_{o,rms}$(W)
6	0	149.9	28.04	2.102
7	30	135.1	26.85	2.002
8	60	120.3	23.79	1.719
9	90	103.9	19.22	1.286

4. EXPERIMENTAL RESULTS AND EVALUATION

4.1. Phase-shift control test results

In this study, experiments were conducted to investigate the effects of PWM phase-shift on the output voltage and current of an inverter in a hot-air drying system. The experimental procedure comprised three main steps: i) PWM phase-shift adjustment, where the phase angle between the output arms of switches S_1 and S_4 was varied in 30° increments at 0°, 30°, 60°, and 90° to evaluate its impact on power delivery, the experimental setup and PWM phase-shift diagram are shown in Figures 9(a) and 9(b); ii) Electrical measurements, in which inverter output voltage and current waveforms were recorded using an oscilloscope, and input power was measured with a power analyzer to determine the supplied power and assess energy conversion efficiency under different phase-shift conditions; and iii) Temperature measurements, where digital thermometers were used to monitor temperatures in the hot-air generation and drying chambers to examine the thermal response to phase-shift variations.

The experimental verification of the phase-shift control strategy and its direct impact on the inverter output is illustrated in Figure 10. The measured waveforms, captured across various phase-shift angles (ϕ), provide a practical correlation between the control signals and the electrical output. As observed in Figures 10(a)–10(d), both the inverter output voltage ($v_{o,rms}$) and current ($i_{o,rms}$) exhibit a consistent decreasing trend as the phase-shift angle increases. Specifically, at $\phi = 0°$ (Figure 10(a)), the system delivers a measured voltage of 132 V and a current of 13.9 A. When the phase angle is adjusted to 90° (Figure 10(d)), these values decrease to 99.5 V and 10.1 A, respectively. This reduction in electrical magnitude demonstrates a corresponding decrease in total output power, thereby validating the expected phase-shift behavior and confirming the effective power regulation capability of the proposed series-resonant inverter system under actual operating conditions.

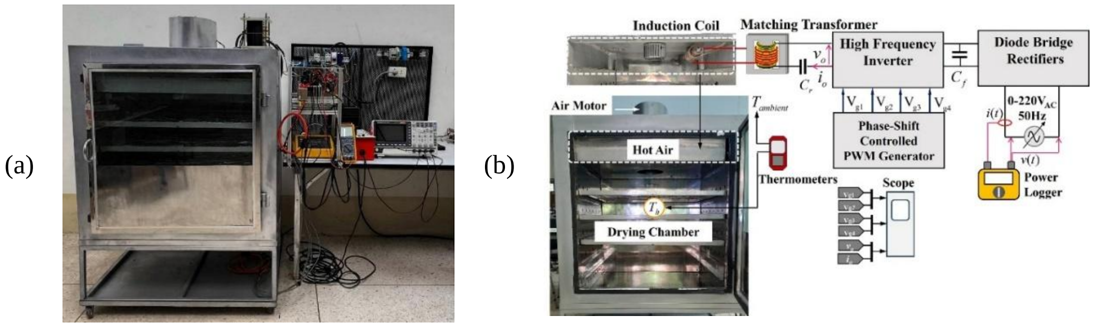

Figure 9. Experimental setup of the series-resonant inverter system and its control synchronization, comparing (a) the physical system prototype and (b) the PWM output phase-shift diagram

Figure 11 illustrates the relationship between phase shift, input power, and power factor of the induction heating system. As the phase shift increases from 0° to 90°, the input power decreases from 2,090 W to 1,270 W, indicating maximum power transfer at zero phase shift and a reduction as the phase displacement grows a typical characteristic of phase-shift control in resonant inverters. Simultaneously, the power factor drops from 0.91 to 0.82 due to the increasing reactive component in the input current, which lowers real power transfer. This inverse correlation between phase shift and both power and power factor reflect the trade-off between output regulation and input power quality in phase-shift controlled induction heating.

Table 4 summarizes the relationship between phase shift, input power, and heating time at a constant target temperature of 55.2 °C. As the phase shift increases, input power declines from 2,009 W to 1,270 W, while heating time extends from 7.18 min to 18.05 min, respectively. This inverse trend indicates that increasing the phase shift reduces power delivery, thereby slowing the system's thermal response.

Table 4. Outlet air temperature during phase-shift adjustment

Phase shift (º)	Pin (W)	Temperature (ºC)	Time (min)
0	2,009	55.2	7.18
30	1,930	55.2	8.33
60	1,706	55.2	9.47
90	1,270	55.2	18.05

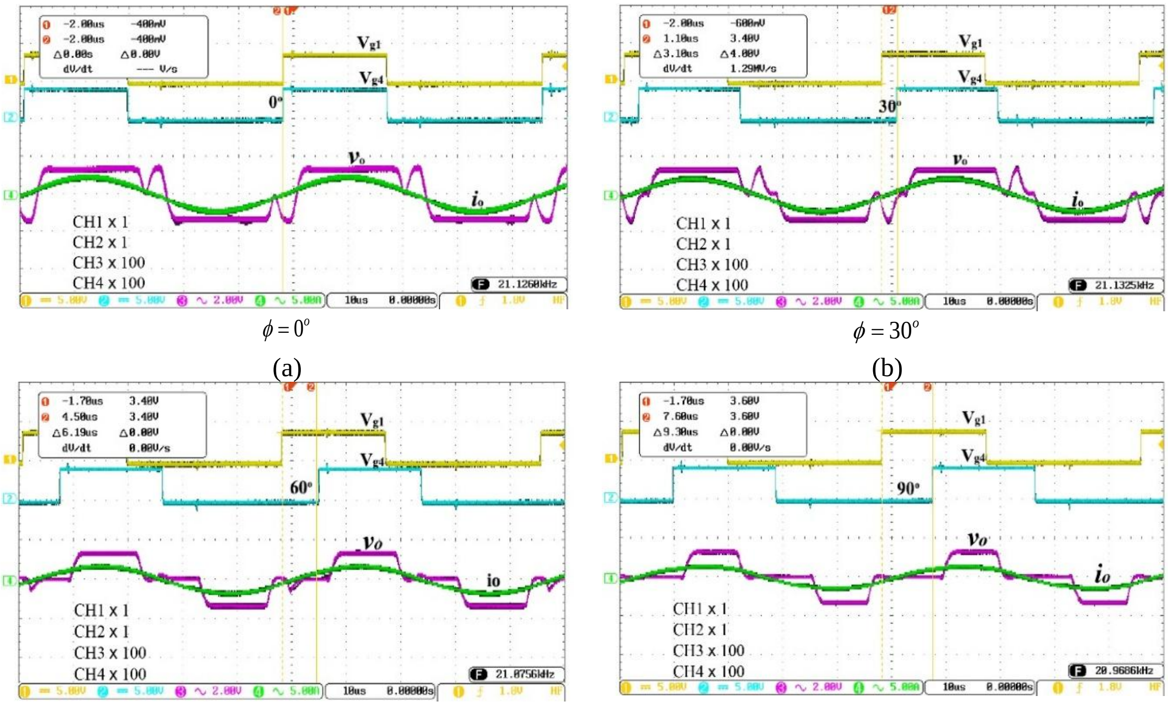

$\phi = 0^o$

(a)

$\phi = 30^o$

(b)

$\phi = 60^o$

(c)

$\phi = 90^o$

(d)

Figure 10. Experimental inverter output voltage and current waveforms at phase-shift angles of (a) φ = 0°, (b) φ = 30°, (c) φ = 60°, and (d) φ = 90°, showing a progressive decrease in output magnitude with increasing phase-shift angle

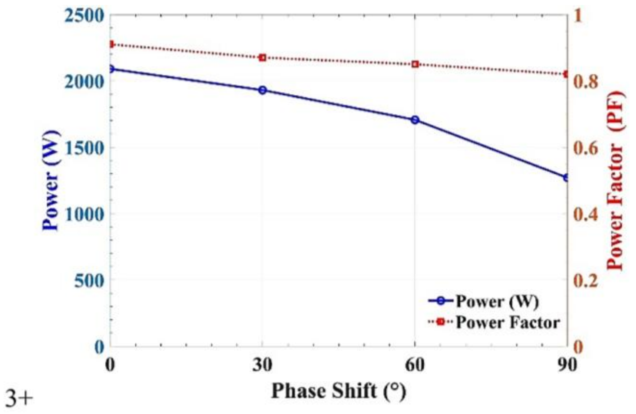

Figure 11. Input power and power factor as a function of phase shift

4.2. Temperature control test results

Temperature in the drying chamber was regulated via a feedback control system to maintain stable conditions. Power input was adjusted based on measured temperatures, ensuring efficient and consistent drying. Control signal waveforms were recorded with an oscilloscope, and input power was measured with a power meter to evaluate energy use. Temperatures in both the heat generation and drying chambers were continuously monitored by sensors. The complete experimental setup is shown in Figure 12.

Figure 13 illustrates hot-air temperature control in the induction-heated drying chamber. Chamber temperature was measured with a K-type thermocouple and processed by a digital controller to command the inverter. Hysteresis control was used with a reference temperature of T_h^* = 55 °C and a band of ΔT = ±1 °C. When temperature falls below $T_h^* - \Delta T$, the phase angle is set to $\phi = 0°$ to increase heating, when it exceeds

$T_h^* + \Delta T$, $\phi = 90°$ to reduce heating. Within 54–56 °C, the system maintains its state to avoid unnecessary switching. This ensures stable temperature, minimal fluctuations, and preserved inverter efficiency. Ambient temperature was approximately 30 °C. Figure 14 presents thermal images of the drying chamber. As shown in Figure 14(a), the actual temperature measurement points (T_h) at the initial stage indicate a rise in temperature to 57 °C within 10 minutes. Following this initial increase, the feedback control system effectively stabilizes the chamber temperature, as illustrated in Figure 14(b), ensuring uniform thermal conditions throughout the drying process.

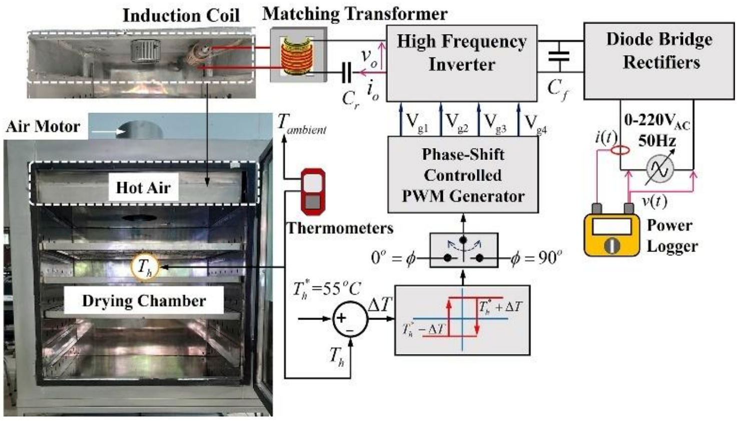

Figure 12. Temperature control diagram of the drying chamber using hysteresis feedback

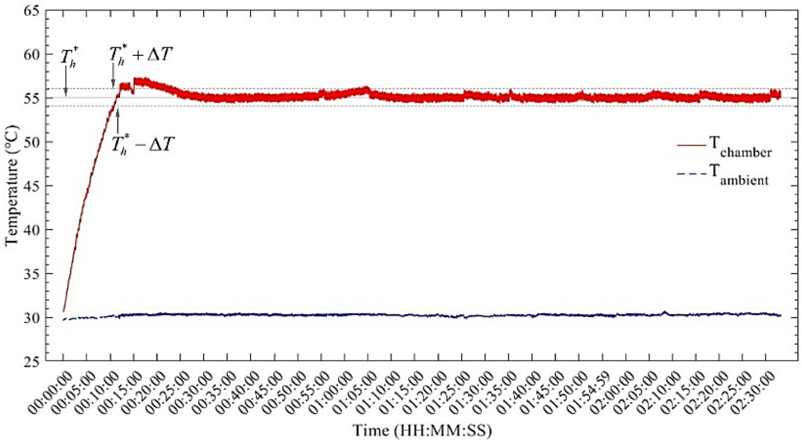

Figure 13. Results of temperature control inside the drying chamber

Figure 15 shows the input voltage and current of the induction heating system. The average root mean square (RMS) voltage was 226 V at startup, with the inverter phase angle set to 0° at 00:00:00, 00:15:00, 00:01:25, 00:01:55, and 00:02:15. The RMS current reached 10.5 A, achieving the set temperature of 55 °C (Figure 13). After stabilization, the phase angle was set to 90°, reducing the RMS current to 5.1 A. Figure 13 presents the input power and power factor, with the inverter initially at 0° at the same time.

The induction heating system reached 2 kW to achieve 55 °C (Figure 13). After stabilization, the inverter phase angle was set to 90°, reducing power to 850 W. The average input RMS voltage and current were 226 V and 10.5 A, respectively, with an average power factor of 0.83. Measured THDv and THDi were 1.5% and 10%, within recommended limits per IEC 61000-2-2 and IEEE 519 (Figure 17) [36], [37].

Energy consumption during the 00:00:00–00:02:30 test period was 2.46 kWh (Figure 18). PWM phase shift adjustments in 30° increments affected performance voltage and current decreased from 132 V and 13.9 A at 0° to 99.5 V and 10.1 A at 90°, respectively, while the power factor remained stable (Figure 11). Phase shift also influenced heating time and power: 0° required 2.07 kW and 7.18 min to reach 55.2 °C, whereas 90° reduced power to 1.15 kW but increased heating time to 18.05 min.

The feedback-controlled drying chamber-maintained temperature within ±1 °C of 55 °C (Figure 13), with minor variations attributed to ambient conditions and heat losses. Input RMS voltage, current, and power factor data (Figures 15 and 16) confirm efficient operation, maintaining a power factor of 0.90 and THDv and THDi within standard limits.

Table 5 compares the energy performance of the induction heating dryer with a conventional hot-air dryer for the same chamber volume. The induction dryer achieved the target temperature of 55 °C in 2.5 hours using 2.46 kWh of active energy, significantly lower than the 3-4 kWh required by conventional dryers. Reactive energy was also reduced to 0.89 kVarh, while precise feedback control minimized temperature fluctuations and heat losses. These results demonstrate that induction heating provides a more energy-efficient and precise drying solution, suitable for industrial applications.

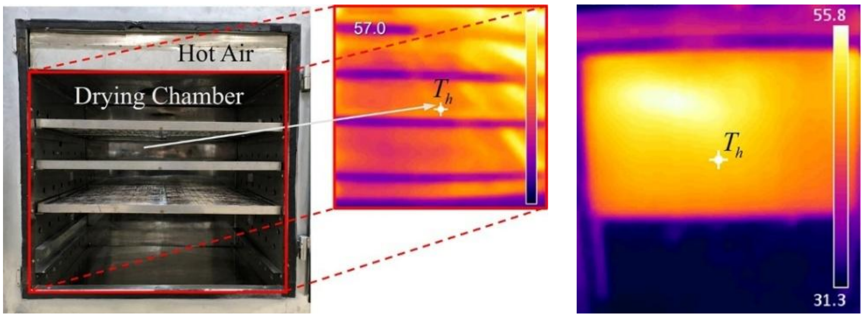

(a) (b)

Figure 14. Analysis of the thermal performance within the drying chamber showing the photograph of the temperature distribution in (a) the side-view profile and (b) the top-view cross-section

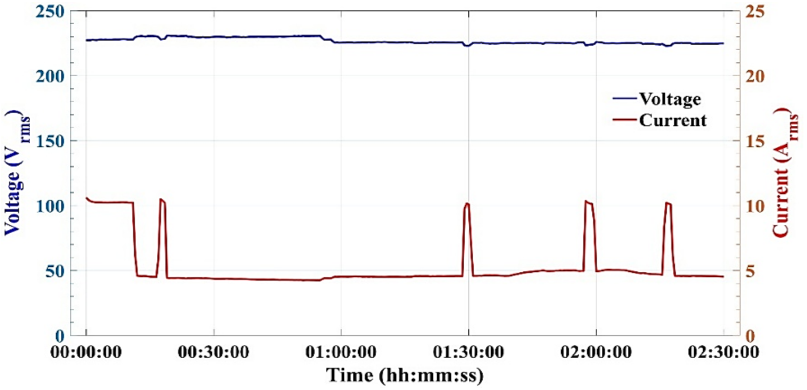

Figure 15. Input voltage and current of the induction heating device

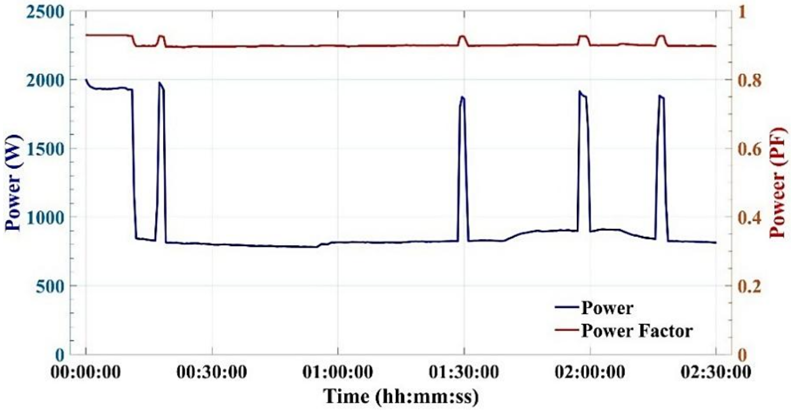

Figure 16. Input power and power factor of the induction heating device

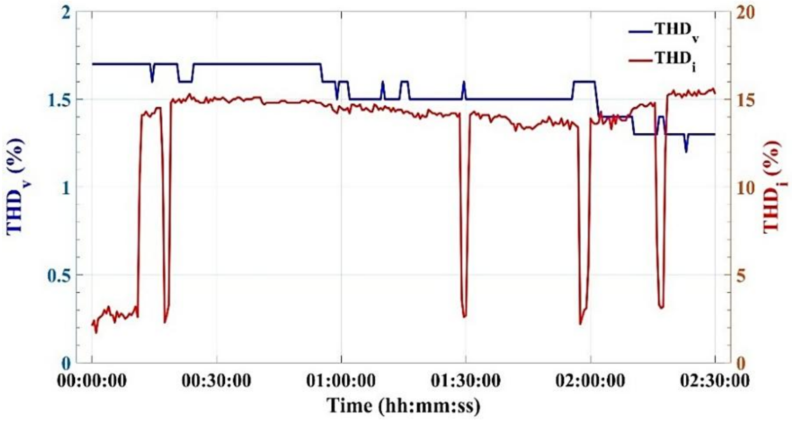

Figure 17. Input THDv and THDi of the induction heating device

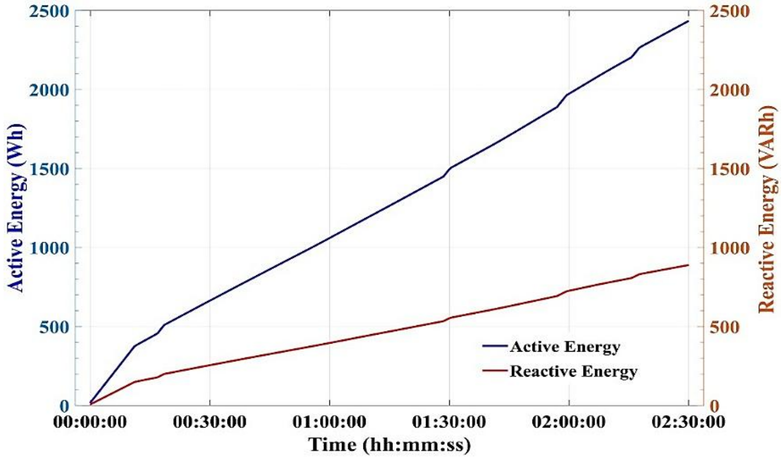

Figure 18. The electric energy consumption rate of the induction heating device

Table 5. Comparison of energy consumption between induction heating and conventional hot-air dryers

Parameter	Induction heating dryer	Conventional hot-air dryer [38], [39]
Chamber dimensions (m × m × m)	0.75×0.62×0.21	0.75×0.62×0.21
Chamber cross-sectional area (m²)	0.04	0.04
Thermal power (kW)	2	3–4
Drying time (h)	2.5	2.5–3
Active energy (kWh)	2.46	3–4
Reactive energy (kVarh)	0.89	1.45
Chamber temperature (°C)	55	55
Ambient temperature (°C)	30	30
Air density (kg/m³)	1.22	1.22
Airflow velocity (m/s)	1.5	1.5
Mass flow rate (kg/s)	0.074	0.074
Advantages	Energy-efficient, fast response, precise temperature control, minimized heat loss	Simple operation, conventional technology, widely used

5. CONCLUSION

This study introduces a novel approach for induction heating dryers by integrating hysteresis control with phase-shifted PWM, marking the first implementation of this combined technique. Experimental results demonstrate that increasing the phase angle reduces output voltage, current, and electrical power consumption while maintaining the power factor within an acceptable range, enabling efficient system operation. The feedback temperature control effectively stabilizes the drying chamber, reflecting the system's adaptability to dynamic conditions. Nonetheless, the energy-saving effect achieved via phase angle adjustment results in extended heating time, highlighting the inherent trade-off between energy efficiency and processing speed. Existing limitations include the controlled laboratory environment, potential mismatches between induction coil design and industrial-scale applications, and constraints of the temperature control system that may require further refinement. Future work should address these gaps by developing intelligent control algorithms, optimizing coil structures, validating performance in real industrial settings, and employing predictive mathematical models. The findings provide a foundational framework for energy-efficient induction heating, offering significant potential for industrial applications in sectors demanding precise thermal management, such as food processing and textile manufacturing. The demonstrated ability to modulate phase angle to enhance system performance underscores the prospect for further innovation in induction heating technology.

FUNDING INFORMATION

The authors would like to acknowledge the support in terms of equipment, instruments, and research facilities provided by the Faculty of Industry and Technology, Rajamangala University of Technology Isan, Sakon Nakhon Campus, Thailand.

AUTHOR CONTRIBUTIONS STATEMENT

This journal uses the Contributor Roles Taxonomy (CRediT) to recognize individual author contributions, reduce authorship disputes, and facilitate collaboration.

Name of Author	**C**	**M**	**So**	**Va**	**Fo**	**I**	**R**	**D**	**O**	**E**	**Vi**	**Su**	**P**	**Fu**
Jeerapong Srivichai	✓	✓	✓	✓	✓	✓		✓	✓	✓			✓	
Kittaya Somsai		✓		✓	✓	✓	✓	✓	✓	✓	✓	✓		
Akkachai Phuphanin		✓	✓		✓	✓	✓	✓	✓	✓	✓	✓		
Nithiroth Pornsuwancharoen	✓		✓	✓	✓	✓			✓	✓	✓		✓	

C : **C**onceptualization
M : **M**ethodology
So : **So**ftware
Va : **Va**lidation
Fo : **Fo**rmal analysis
I : **I**nvestigation
R : **R**esources
D : **D**ata Curation
O : Writing - **O**riginal Draft
E : Writing - Review & **E**diting
Vi : **Vi**sualization
Su : **Su**pervision
P : **P**roject administration
Fu : **Fu**nding acquisition

CONFLICT OF INTEREST STATEMENT

The authors declare that they have no known competing financial interests or personal relationships that could have appeared to influence the work reported in this paper.

DATA AVAILABILITY

Data availability is not applicable to this paper as no new data were created or analyzed in this study.

REFERENCES

[1] A. H. El-Hag, R. Dadarwal, O. R. Gonzalez, S. H. Jayaram, and M. W. Griffiths, “Survivability of inoculated versus naturally grown bacteria in apple juice under pulsed electric fields,” *IEEE Transactions on Industry Applications*, vol. 46, no. 1, pp. 9–15, Feb. 2010, doi: 10.1109/TIA.2009.2036513.

[2] N. O. Kurdyukova, I. V. Ognev, and K. B. Kunanbayeva, “Implementation of machine vision and other automated systems to ensure the collection of representative statistics of process control and quality management at industrial enterprises,” in *Proceedings of the 2021 IEEE International Conference “Quality Management, Transport and Information Security, Information Technologies”, T and QM and IS 2021*, Yaroslavl, Russian Federation, 2021, pp. 309–312. doi: 10.1109/ITQMIS53292.2021.9642904.

[3] J. M. Tabora *et al.*, “Assessing energy efficiency and power quality impacts due to high-efficiency motors operating under nonideal energy supply,” *IEEE Access*, vol. 9, pp. 121871–121882, Sep. 2021, doi: 10.1109/ACCESS.2021.3109622.

[4] A. Chen, Z. Ren, Z. Fan, and X. Feng, “Dead band zone model predictive control of cut tobacco drying process,” *IEEE Access*, vol. 8, pp. 157781–157792, Aug. 2020, doi: 10.1109/ACCESS.2020.3020469.

[5] Z. Guo, J. Xu, Z. Xu, M. Mubashir, H. Wang, and X. Mei, “A three-heat-source electro-thermal coupled model for fast estimation of the temperature distribution of a lithium-ion battery cell,” *IEEE Transactions on Transportation Electrification*, vol. 8, no. 1, pp. 288–297, Mar. 2022, doi: 10.1109/TTE.2021.3095288.

[6] P. Y. Liao *et al.*, “Energy consumption and carbon emission reduction in HVAC system of a dynamic random access memory (dram) semiconductor fabrication plant (fab),” *IEEE Transactions on Semiconductor Manufacturing*, vol. 37, no. 2, pp. 174–184, May 2024, doi: 10.1109/TSM.2024.3379949.

[7] Z. Zhang, Q. Jiang, C. Zhou, and X. Liu, "Strength and failure characteristics of Jurassic red-bed sandstone under cyclic wetting-drying conditions," *Geophysical Journal International*, vol. 198, no. 2, pp. 1034–1044, May 2014, doi: 10.1093/gji/ggu181.

[8] S. H. Alyami, A. A. Almutlaqa, A. M. Alqahtany, and N. Ashraf, "Likelihood of reaching zero energy building design in hot dry climate: saudi arabia," *IEEE Access*, vol. 9, pp. 167054–167066, Dec. 2021, doi: 10.1109/ACCESS.2021.3134365.

[9] B. Satpati, C. Koley, and S. Datta, "Sensor-less predictive drying control of pneumatic conveying batch dryers," *IEEE Access*, vol. 5, pp. 3547–3568, Mar. 2017, doi: 10.1109/ACCESS.2017.2675625.

[10] R. A. Lone and M. A. Bhat, "Impact of quality on customer satisfaction: evidence from selected consumer durables," *International Journal for Research Trends and Innovation*, vol. 8, no. 4, pp. 1014–1024, Apr. 2023.

[11] H. Liu, E. Miao, L. Zhang, L. Li, Y. Hou, and D. Tang, "Thermal error modeling for machine tools: mechanistic analysis and solution for the pseudo correlation of temperature-sensitive points," *IEEE Access*, vol. 8, pp. 63497–63513, Apr. 2020, doi: 10.1109/ACCESS.2020.2983471.

[12] R. Liu, L. Li, and Y. Yang, "Performance residual-based fault detection for feedback control systems," *IEEE Transactions on Circuits and Systems II: Express Briefs*, vol. 68, no. 10, pp. 3291–3295, Oct. 2021, doi: 10.1109/TCSII.2021.3062718.

[13] A. Parastiwi, and Ekojono, "Design of spray dryer process control by maintaining outlet air temperature of spray dryer chamber," *International Seminar on Intelligent Technology and Its Applications (ISITIA)*, Lombok, Indonesia, pp. 619–622, 2016, doi: 10.1109/ISITIA.2016.7828731.

[14] S. Gowshmeed, R. Vithiya, and E. Ramassamy, "Pulsed electric field for food preservation," in *Proceedings International Conference on System, Computation, Automation and Networking (ICSCAN)*, Puducherry, India, pp. 1–5, Nov. 2023, doi: 10.1109/ICSCAN58655.2023.10395041.

[15] E. Atam, D. Patteeuw, S. P. Antonov, and L. Helsen, "Optimal control approaches for analysis of energy use minimization of hybrid ground-coupled heat pump systems," *IEEE Transactions on Control Systems Technology*, vol. 24, no. 2, pp. 525–540, Mar. 2016, doi: 10.1109/TCST.2015.2445851.

[16] A. S. Afifah, I. W. K. Suryawan, M. R. Apritama, G. Prajati, and Y. Adicita, "Kinetics of organic and nutrient degradation with microalgae biomass cultured in photobioreactors," in *Proceeding's 2nd International Conference on Applied Engineering (ICAE)*, Batam, Indonesia, 2019, pp. 1–4, doi: 10.1109/ICAE47758.2019.9221749.

[17] H. Wang, A. S. Pierre, and P. Mancarella, "System level cost and environmental performance of integrated energy systems: An assessment of low-carbon scenarios for the UK," in *Proceedings IEEE Eindhoven Power Tech, Eindhoven,* Netherlands, pp. 1–6, Feb. 2016, doi: 10.1109/PTC.2015.7232659.

[18] W. Suchonpanit, Y. Tirawanichakul, and S. Tirawanichakul, "Experimental study of the effects of different drying methods on the kinetics and quality of air-dried sheet (ADS) rubber," *IEEE Colloquium on Humanities, Science and Engineering,* Penang, Malaysia, vol. 1, pp. 202–207, 2011, doi: 10.1109/CHUSER.2011.6163717.

[19] V. Rudnev, D. Loveless, and R. L. Cook, *Handbook of induction heating, second edition*. New York, USA: Marcel Dekker, Inc., 2017. doi: 10.1201/9781315117485.

[20] C. H. Chan, Y. A. Yusof, and N. L. Chin, "Induction heating in food processing and drying: a review," *Food Engineering Reviews*, vol. 11, no. 3, pp. 135–158, 2019.

[21] ASM International, *ASM handbook: heat treating*. Materials Park, OH, USA: ASM International, 1999.

[22] H. Toğrul, "Suitable drying model for infrared drying of carrot," *Journal of Food Engineering*, vol. 77, no. 3, pp. 610–619, Dec. 2006, doi: 10.1016/j.jfoodeng.2005.07.020.

[23] N. Pleshivtsev, "Mathematical modelling of induction heating processes," *Journal of Materials Processing Technology*, vol. 40, no. 1--2, pp. 347–355, 1994.

[24] Y. A. Cengel and M. A. Boles, *Thermodyamics an engineering approach*, 4th ed., vol. 1. New York, USA: McGraw-Hill College, 2002. [Online]. Available: http://www.ulb.tu-darmstadt.de/tocs/182108600.pdf

[25] B. Y. Chen and Y. S. Lai, "Switching control technique of phase-shift-controlled full-bridge converter to improve efficiency under light-load and standby conditions without additional auxiliary components," *IEEE Transactions on Power Electronics*, vol. 25, no. 4, pp. 1001–1012, Apr. 2010, doi: 10.1109/TPEL.2009.2033069.

[26] M. Zhang, S. Wang, Y. Sun, Z. Guo, and J. Bao, "A phase-shifted full-bridge converter used for dc charging pile," in *IOP Conference Series: Materials Science and Engineering*, IOP Publishing, 2020. doi: 10.1088/1757-899X/768/6/062010.

[27] R. Viswadev, A. Mudlapur, V. V. Ramana, B. Venkatesaperumal, and S. Mishra, "A novel ac current sensorless hysteresis control for grid-tie inverters," *IEEE Transactions on Circuits and Systems II: Express Briefs*, vol. 67, no. 11, pp. 2577–2581, Nov. 2020, doi: 10.1109/TCSII.2019.2960289.

[28] A. Dey, S. Patra, and S. Sen, "Integral control of stable negative-imaginary systems preceded by hysteresis nonlinearity," *IEEE Transactions on Automatic Control*, vol. 65, no. 3, pp. 1333–1339, Mar. 2020, doi: 10.1109/TAC.2019.2930228.

[29] M. Kurre and A. Banerjee, "Zero voltage switching self-oscillating PWM inverter in induction heating applications," *Journal of Engineering Research*, vol. 1, pp. 1–15, 2022, doi: 10.36909/jer.16717.

[30] B. Meziane and H. Zeroug, "Comprehensive power control performance investigations of resonant inverter for induction metal surface hardening," *IEEE Transactions on Industrial Electronics*, vol. 63, no. 10, pp. 6086–6096, 2016, doi: 10.1109/TIE.2016.2581145.

[31] R. W. Erickson, and D. Maksimovic, *Fundamentals of power electronics*, 2nd ed., Kluwer Academic Publishers, 2001. doi: 10.1007/978-1-4471-5104-3_2.

[32] M. H. Rashid, *Power electronics handbook*, 4th ed. Elsevier, 2011. doi: 10.1016/c2016-0-00847-1.

[33] A. Attab, H. Zeroug, and C. Hammouma, "Investigations into series resonant inverter power control parameters for an effective metal induction surface hardening," *IET Electric Power Applications*, vol. 14, no. 6, pp. 1097–1107, 2020, doi: 10.1049/iet-epa.2018.5740.

[34] Y. S. Kwon, S. B. Yoo, and D. S. Hyun, "Half-bridge series resonant inverter for induction heating applications with load-adaptive pfm control strategy," in *Conference Proceedings - IEEE Applied Power Electronics Conference and Exposition - APEC*, 1999, pp. 575–581. doi: 10.1109/apec.1999.749738.

[35] Y. Kawaguchi, E. Hiraki, T. Tanaka, and M. Nakaoka, "Basic study of a phase-shifted soft switching high-frequency inverter with boost pfc converter for induction heating," *Journal of Power Electronics*, vol. 8, no. 2, pp. 192–199, 2008.

[36] IEC, "IEC 61000-2-2: electromagnetic compatibility (EMC) – environment – compatibility levels for low-voltage power supply systems," 2017. [Online]. Available: https://cdn.standards.iteh.ai/samples/19695/e206f099a068466293d5cce764583de4/IEC-61000-2-2-2002-AMD1-2017.pdf.

[37] IEEE, "IEEE recommended practice and requirements for harmonic control in electric power systems," *IEEE Std. 519-2014*, vol. 2014. IEEE, p. New York, 2014.

[38] A. S. Mujumdar, *Handbook of industrial drying*, 4th ed. CRC Press, 2020. doi: 10.1201/9780429289774.

[39] I. T. Togrul and D. Pehlivan, “Drying of foods: modelling and numerical analysis,” *Journal of Food Engineering*, vol. 61, pp. 359–369, 2004.

BIOGRAPHIES OF AUTHORS

Jeerapong Srivichai received the B.Eng. degree in electrical engineering from Pathumwan Institute of Technology, Bangkok, Thailand, in 2003, the M.Eng. degree in electrical engineering from Kasetsart University, Bangkok, Thailand, in 2008, and the Ph.D. degree in electrical engineering from Suranaree University of Technology, Nakhon Ratchasima, Thailand, in 2020. He is currently an assistant professor with the Department of Electrical Engineering, Rajamangala University of Technology Isan Sakon Nakhon Campus, Sakon Nakhon, Thailand. His research interests include railway electrification, electric vehicles, power electronics, and induction heating. He can be contacted at email: geerapong.sr@rmuti.ac.th.

Kittaya Somsai received the B.Eng. degree in electrical engineering from Rajamangala Institute of Technology, Thailand, in 2003, the M.Eng. degree in electrical engineering from King Mongkut's Institute of Technology North Bangkok, Thailand, in 2005, and the Ph.D. degree in electrical engineering from Suranaree University of Technology, Thailand, in 2012. He is currently an Assistant Professor with the Department of Electrical Engineering, Rajamangala University of Technology Isan Sakon Nakhon Campus, Thailand. His research interests include power systems, custom power devices, power electronics and control, and artificial intelligence techniques. He can be contacted at email: kittaya.so@rmuti.ac.th.

Akkachai Phuphanin received the B.Eng., M.Eng., and Ph.D. degrees in telecommunication engineering from Suranaree University of Technology, Thailand, in 2009, 2011, and 2017, respectively. He is currently a Lecturer with the Department of Electrical Engineering, Rajamangala University of Technology Isan Sakon Nakhon Campus, Thailand. His research interests include wireless sensor networks and applications, smart farm and home technology, coverage control, the internet of things, and signal processing. He can be contacted at email: akkachai.ph@rmuti.ac.th.

Nithiroth Pornsuwancharoen received the B.S.Tech.Ed., M.S.Tech.Ed., and Ph.D. degrees in telecommunication engineering and applied physics from King Mongkut’s Institute of Technology Ladkrabang, Bangkok, Thailand, in 1998, 2005, and 2009, respectively. He is currently a Lecturer with the Department of Electrical Engineering, Faculty of Industry and Technology, Rajamangala University of Technology Isan Sakon Nakhon Campus, Sakon Nakhon, Thailand. His research interests include fast charging, electronic circuits, micro-ring resonators, soliton communication, IoT, and quantum communication. He can be contacted at email: nithiroth.po@rmuti.ac.th.